
HWC-LoCo: A Hierarchical Whole-Body Control Approach to Robust Humanoid Locomotion

Sixu Lin^{1,2} Guanren Qiao¹ Yunxin Tai³ Ang Li^{1,4} Kui Jia^{1,3} Guiliang Liu¹

Abstract

Humanoid robots, capable of assuming human roles in various workplaces, have become essential to the advancement of embodied intelligence. However, as robots with complex physical structures, learning a control model that can operate robustly across diverse environments remains inherently challenging, particularly under the discrepancies between training and deployment environments. In this study, we propose HWC-LoCo, a robust whole-body control algorithm tailored for humanoid locomotion tasks. By reformulating policy learning as a robust optimization problem, HWC-LoCo explicitly learns to recover from safety-critical scenarios. While prioritizing safety guarantees, overly conservative behavior can compromise the robot’s ability to complete the given tasks. To tackle this challenge, HWC-LoCo leverages a hierarchical policy for robust control. This policy can dynamically resolve the trade-off between goal-tracking and safety recovery, guided by human behavior norms and dynamic constraints. To evaluate the performance of HWC-LoCo, we conduct extensive comparisons against state-of-the-art humanoid control models, demonstrating HWC-LoCo’s superior performance across diverse terrains, robot structures, and locomotion tasks under both simulated and real-world environments. Our project page is available at: https://simonlinsx.github.io/HWC_Loco/.

1. Introduction

Humanoid robots, with a physical structure resembling that of humans, can be seamlessly integrated into humans’ workspace and take on roles in completing different tasks (Saeedvand et al., 2019). This capability makes them

¹The Chinese University of Hong Kong (Shenzhen) ²Harbin Institute of Technology (Shenzhen) ³DexForce Technology ⁴Southeast University. Correspondence to: Guiliang Liu <liuguiliang@cuhk.edu.cn>.

Preprint.

reliable embodiments of artificial intelligence in various forms (Paolo et al., 2024). In recent years, with advancements in both hardware capabilities and control algorithms, humanoid robots have become an increasingly significant type of robot with a growing impact on practical applications across various environments, such as factories, homes, and offices (Sferrazza et al., 2024; Nasiriany et al., 2024; Tao et al., 2024). However, humanoid robots are typically equipped with complex upper and lower body designs that involve numerous degrees of freedom. Developing robust control algorithms that allow these robots to adapt to a wide range of environments remains a significant challenge.

In the development of humanoid control policy, classic methods commonly rely on model-based optimization (Sakagami et al., 2002; Sentis & Khatib, 2006; Gouaillier et al., 2009; Radford et al., 2015; Chignoli et al., 2021). However, these methods require precise and comprehensive modeling of the robot’s structure, kinematics, and dynamics across different environments. In practice, obtaining such data requires significant computational resources or manual effort. These limitations significantly influence the scalability of these approaches. To develop an end-to-end solution with promising generalizability, recent studies (Zhuang et al., 2024; Radosavovic et al., 2024; Long et al., 2024; He et al., 2024b; Gu et al., 2024b) adopted Reinforcement Learning (RL) methods by training a neural model to control based on human demonstrations and interactions with the environment.

While these learning-based approaches show potential for effective control policies across various tasks, they are typically trained in simulated environments, which often differ considerably from the deploying environment. To bridge the Simulation-to-Real (Sim2Real) gap, previous works often introduce additional regularization to constrain the robot’s movements or employ domain randomization to account for variations in the robot’s physical properties (Lai et al., 2023; Rudin et al., 2022; Nahrendra et al., 2023). However, excessive regularization can greatly affect the efficiency of control policy, and unstructured randomization often fails to capture safety-critical patterns in real-world applications.

To develop a reliable locomotion policy capable of generalizing from the training to the deployment environment, we propose formulating policy optimization as a robust

optimization problem under misspecified environmental dynamics. However, traditional robust optimization primarily focuses on worst-case control, requiring the policy to ensure safety under the most adverse environmental dynamics within an uncertainty set. Under this context, the learned policy tends to be overly conservative, inducing sub-optimal control performance in terms of finishing the given task.

In this paper, to learn a control policy that can dynamically solve the trade-off between maximizing performance and maintaining safety under different deployment environments, we present a **Hierarchical Whole-body Control for Robust Humanoid Locomotion (HWC-LoCo)** that seamlessly incorporates the following policies:

The *goal-tracking policy* is designed to follow task-specific commands (e.g., moving velocity and direction). Additionally, we ensure that the learned policy can effectively adhere to humanoid behavioral patterns by ensuring its distributional alignment with human motions. Note that this policy primarily focuses on ensuring task completion performance, without addressing safety issues that may arise from potential mismatches with the deployment environment.

The *safety-recovery policy* aims at ensuring safety across various deployment environments. To address safety-critical scenarios during deployment, we construct an uncertainty set by designing an extreme-case estimation mechanism. Within these constructed scenarios, we propose a dynamic constraint guided by Zero Moment Points (ZMPs) to effectively identify safe control policies. By evaluating whether the ZMPs remain within the support surface, HWC-LoCo can assess and ensure the stability of bipedal robots.

While the goal-tracking and safety-recovery policies are primarily designed to enhance task performance and safety control, respectively, they lack a coordination mechanism to effectively control the trade-off between these objectives. To address this limitation, we propose a *high-level planning policy* that dynamically selects which policy to activate based on the deployment scenario.

We conduct extensive experiments to evaluate the performance of HWC-LoCo from four fundamental perspectives: 1) *scalability*, demonstrated across diverse terrains and robot embodiments, 2) *robustness*, evaluated under varying scales of environmental disturbances, 3) *naturalness*, exhibited in its ability to imitate human behavioral norms and movements, and 4) *sensitivity* reflected in its dynamic adjustment of the low-level policies’ activation rates based on environmental conditions. These validations are performed in both simulated and real-world settings, demonstrating HWC-LoCo as a foundational advancement for achieving reliable humanoid locomotion in safety-critical scenarios.

2. Related Work

Learning-based Legged Robot Locomotion. Various learning-based methods have been proposed for legged locomotion, such as quadrupedal locomotion (Rudin et al., 2022; Shi et al., 2022; Chen et al., 2023; Nahrendra et al., 2023; Margolis & Agrawal, 2023; Zhuang et al., 2023) and bipedal locomotion (Li et al., 2021; Kumar et al., 2022; Li et al., 2023; Duan et al., 2024). Besides, recent studies (He et al., 2024d; Tan et al., 2023) have investigated the design of hierarchical controllers, where a high-level policy guides the lower-level action policy of quadrupedal robots. Despite their success, these approaches cannot be directly applied to humanoid robots because of their complex physical structure and the higher degrees of freedom. Recent advances in hardware and learning methods (e.g., RL algorithms) have enabled humanoid robots to move through diverse and complex environments. Some humanoid control policy navigates across diverse terrains using only proprioceptive information (Radosavovic et al., 2024; Gu et al., 2024c;b). Others enhance performance by incorporating additional sensors, such as vision or LiDAR, to collect detailed environmental data, enabling robots to perform complex tasks like stair climbing and parkour jumps (Zhuang et al., 2024; Long et al., 2024). While these approaches have demonstrated promising locomotion performance, they lack mechanisms to handle safety-critical scenarios that humanoid robots may encounter during real-world deployment.

Whole-body control for humanoid robots. Learning to perform whole-body control remains a critical goal for humanoid robots. By leveraging prior motion trajectories, recent studies (Cheng et al., 2024; He et al., 2024b;a; Fu et al., 2024; He et al., 2024c) have enabled robots to learn human-like movements, such as boxing and dancing. Additionally, previous methods employed multi-stage reward designs to accomplish complex tasks (Kim et al., 2024; Zhang et al., 2024a). These methods have demonstrated the importance of coordinating interactions between the upper and lower body. However, the success of these methods often relies on intricate reward shaping and struggles to generalize across different humanoid robots, particularly when motion priors are unavailable.

3. Problem Formulation

Partially Observable Markov Decision Process. We formulate the environment of humanoid locomotion task with a Partially Observable Markov Decision Process (POMDP) $M = (\mathcal{S}, \mathcal{A}, \mathcal{O}, P_{\mathcal{T}}, r, \mu_0, \gamma)$, where: 1) Within the state space \mathcal{S} , a state $s \in \mathcal{S}$ records the complete environmental information and the robot’s internal states. 2) \mathcal{A} denotes the action space, and action $a \in \mathcal{A}$ denotes the target joint angles that a PD controller uses to actuate the degrees of freedom (DOF). 3) \mathcal{O} denotes the partial observations $o \in \mathcal{O}$, which provide incomplete information

about the state of the agent due to sensory limitations and environmental uncertainty. At a time step t , \mathbf{o}_t includes velocity command $\mathbf{v}_t^{cmd} \in \mathbb{R}^3$ and proprioception \mathbf{o}_t^p that records a humanoid’s internal state. Appendix A.2 introduces the details. By incorporating the temporal observations $\mathbf{o}_t^H = [\mathbf{o}_t, \mathbf{o}_{t-1}, \dots, \mathbf{o}_{t-H}]$, the control model can summarize a state as $s_t = [\mathbf{o}_t^H, \mathbb{P}_t]$, where \mathbb{P}_t is the privileged information which the robot can’t access in realistic deployment, including base velocity v_t , terrain height, external disturbance and ZMP features (see Section 4.3). 4) r denotes the reward functions, which typically consist of penalty, regularization, and task rewards. These reward signals significantly influence the optimality of the control policy, for which we provide a detailed introduction in the following. 5) $P_{\mathcal{T}} \in \Delta_{\mathcal{S} \times \mathcal{A}}^{\mathcal{S}}$ denotes the transition function as a mapping from state-action pairs to a distribution of future states. 6) $\mu_0 \in \Delta^{\mathcal{S}}$ denotes the initial state distribution. 7) $\gamma \in (0, 1]$ denotes the discounting factor. The planning stops at a terminating state \bar{s} , and the corresponding terminating time is denoted as $T \in (0, \infty)$.

Under this POMDP, our goal of humanoid locomotion is to learn a policy $\pi \in \Delta_{\mathcal{S}}^{\mathcal{A}}$ according to the objective as follows:

$$\mathcal{J}(\pi, M) = \mathbb{E}_{\mu_0, P_{\mathcal{T}}, \pi} \left[\sum_{t=0}^{\infty} \gamma^t r(s_t, a_t) \right] \quad (1)$$

In the task of humanoid locomotion, the total rewards can be generally represented as a weighted combination of task rewards $r_{\mathcal{T}}$, penalty rewards $r_{\mathcal{P}}$, and regularization rewards $r_{\mathcal{R}}$ (He et al., 2024b;a; Zhuang et al., 2024):

$$r(s_t, a_t) = \beta_{\mathcal{T}} r_{\mathcal{T}}(s_t, a_t) + \beta_{\mathcal{P}} r_{\mathcal{P}}(s_t, a_t) + \beta_{\mathcal{R}} r_{\mathcal{R}}(s_t, a_t)$$

where the rewards have distinct semantic meanings:

- *Task rewards* $r_{\mathcal{T}}$ assess how effectively the agents achieve the goals of the current task, such as tracking velocities (Zhuang et al., 2024), managing contacts (Zhang et al., 2024a), and producing expressive motions (Cheng et al., 2024). These task rewards are closely correlated with the optimality of the current control policy, making them an appropriate *objective to maximize* in this context.
- *Penalty rewards* $r_{\mathcal{P}}$ are used to prevent undesirable events. For example, in locomotion tasks, these penalties are applied when the humanoid falls or when the robot violates dynamic constraints, such as torque limits and joint position limits. To mitigate these negative outcomes, recent studies (He et al., 2024b;a) have assigned a large weight $\beta_{\mathcal{P}}$ to these rewards. However, we find that these empirical weights inherently function as Lagrange multipliers in constrained optimization problems (Gu et al., 2024a). Consequently, a more effective approach would be to model the control problem as a *constrained RL problem*.
- *Regularization rewards* $r_{\mathcal{R}}$ are used to align the behavior of the humanoid with human preferences regarding

motion styles, safe deployment, and other kinematic or dynamic concerns. However, accurately specifying these regularizations remains challenging since they are often task-dependent, context-sensitive, and inherently rooted in human experts’ experience (Chen et al., 2024). As a result, instead of manually specifying regularizations, we *align the robot’s motion with human preferences* by imitating human behavior from motion datasets (e.g., AMASS dataset (Mahmood et al., 2019)), which contains rich signals about desirable behavior norms.

Constrained RL for Whole-Body Control. Inspired by the aforementioned analysis, we formulate the whole-body control locomotion objective for humanoid robots as follows:

$$\begin{aligned} \max_{\pi} \mathcal{J}(\pi, M) &= \max_{\pi} \mathbb{E}_{\mu_0, P_{\mathcal{T}}, \pi} \left[\sum_{t=0}^{\infty} \gamma^t r_{\mathcal{T}}(s_t, a_t) \right] \quad (2) \\ \text{s.t. } \mathcal{D}_f(\rho_M^{\pi^E} \parallel \rho_M^{\pi}) &\leq \epsilon_f \text{ and } \mathbb{E}_{\tau \sim (\mu_0, P_{\mathcal{T}}, \pi)} [\phi(\tau)] \geq \epsilon_{\phi} \end{aligned}$$

where 1) we replace the hard regularization in $r_{\mathcal{R}}$ with a mimic learning objective $\mathcal{D}_f(\rho_M^{\pi^E} \parallel \rho_M^{\pi})$ that constrains the distributional divergence between the learned policy’s occupancy measure ρ_M^{π} and the expert policy’s occupancy measure $\rho_M^{\pi^E}$. In this study we implement \mathcal{D}_f by Wasserstein distance (Section 4.1). 2) Instead of relying on the penalty reward $r_{\mathcal{P}}$, we use ϕ to capture the feasibility of the current trajectory generated by the policy π under the environment M . Within the objective, only the task rewards $r_{\mathcal{T}}$ are subject to maximization; other desired characteristics of humanoid robots are captured by constraints learned from human motion datasets. More importantly, this approach effectively eliminates the need for regularization on the humanoid robot’s upper or lower pose, significantly enhancing the learning of whole-body locomotion policies.

Robust Locomotion in Humanoid Robot. A common approach to learning humanoid locomotion policies involves training in a simulated environment before deploying the policies in a real-world setting. Due to the complexity of real-world environments, there is often a significant discrepancy between the training and deployment environments. In this study, we characterize this discrepancy by the mismatched POMDPs defined as follows:

Definition 3.1. (Mismatched POMDPs) We define a POMDP $M := (\mathcal{S}, \mathcal{A}, P_{\mathcal{T}}, \mathcal{O}, r, \mu_0, \gamma)$, to be mismatched with another POMDP $M' := (\mathcal{S}, \mathcal{A}, P'_{\mathcal{T}}, \mathcal{O}, r, \mu_0, \gamma)$ if they differ only in transition functions (i.e., $P_{\mathcal{T}} \neq P'_{\mathcal{T}}$). We define a set of mismatched POMDPs as $\mathcal{M}_m = \{M^{P_{\mathcal{T}}}, M^{P'_{\mathcal{T}}}, \dots\}$, where their transition functions differ from each other.

Note that we follow previous studies (Moos et al., 2022) and primarily focus on the mismatch in transition dynamics during learning and deployment. The uncertainty set of

transition function (Viano et al., 2022) is represented as:

$$\mathfrak{P}_\alpha^L = \{\alpha P_{\mathcal{T}}^L + (1 - \alpha)\bar{P}_{\mathcal{T}}, \forall \bar{P}_{\mathcal{T}} \in \mathfrak{P}\} \quad (3)$$

where α specifies the scale of mismatch, $P_{\mathcal{T}}^L$ denotes the transition function in the learning environment and $\mathfrak{P} \subseteq \Delta_{S \times \mathcal{A}}^S$ represents the set of all candidate transition functions. While other factors, such as divergence in state-action spaces and initial state distribution μ_0 , can influence the performance during deployment, we find that the majority of factors affecting Sim2Real performance in humanoid locomotion tasks can be characterized by the mismatch in transition dynamics. For example, if $P_{\mathcal{T}}$ denotes a Gaussian function, the underlying sensor noise can be captured by transitions in \mathfrak{P}_α^L . Additionally, if $\bar{P}_{\mathcal{T}}$ denotes a projection from one spatial state to another, the variations of terrains in the deploying environment can be modeled by transitions in \mathfrak{P}_α^L (Long et al., 2024).

To solve a robust RL problem, previous studies often consider a max-min objective $\max_{\pi} \min_{M \in \mathcal{M}_m} \mathcal{J}(\pi, M)$ where $\mathcal{J}(\pi, M)$ denotes a standard RL objective (1). With this objective, while the agent can learn a conservative policy to ensure worst-case control performance, this policy often compromises the control performance, making the humanoid less effective at tracking the given commands. To address this issue, we focus on ensuring a worst-case feasibility constraint, thereby reducing the influence of mismatched POMDP on maximizing task rewards. Accordingly, we update the CRL objective (2) to the robust humanoid locomotion objective represented as follows:

$$\begin{aligned} \max_{\pi} \min_{\bar{P}_{\mathcal{T}} \in \mathfrak{P}_\alpha^L} \mathbb{E}_{\mu_0, P_{\mathcal{T}}^L, \pi} \left[\sum_{t=0}^{\infty} \gamma^t r_{\mathcal{T}}(s_t, a_t) \right] \\ \text{s.t. } \mathcal{D}_f(\rho_M^{\pi^E} \parallel \rho_M^{\pi}) \leq \epsilon_f \text{ and } \mathbb{E}_{\tau \sim (\mu_0, \bar{P}_{\mathcal{T}}, \pi)} [\phi(\tau)] \geq \epsilon_\phi \end{aligned} \quad (4)$$

where 1) \mathfrak{P}_α^L represents the set of mismatched dynamics from the learning environment dynamics $P_{\mathcal{T}}^L$ (defined in 3) and 2) $\rho_M^{\pi}(s, a) = (1 - \gamma)\pi(a|s) \sum_{t=0}^{\infty} \gamma^t p(s_t = s | \pi, M)$ defines the normalized occupancy measure of policy π under the environment M . Intuitively, we aim to learn a robust control policy that ensures feasibility across all mismatched transition functions $\bar{P}_{\mathcal{T}} \in \mathfrak{P}_\alpha^L$, thereby guaranteeing the safety of policy π . However, for the reward-maximizing and mimic learning objectives, we optimize the policy based on the transition dynamics in the learning environment $P_{\mathcal{T}}^L$, rather than concentrating solely on worst-case guarantees.

4. Hierarchical Whole-Body Control for Humanoid Robust Locomotion

In practice, developing an end-to-end solver for the robust locomotion problem (4) is challenging, as it involves multiple deployment environments and constraints that must be adhered to. To tackle this issue, we propose dividing the

objective into two stages: goal-tracking and safety recovery. The goal-tracking policy maximizes rewards while mimicking human behaviors (see Section 4.1). When mismatched environmental dynamics pose a risk to the safety of the control policy, HWC-LoCo switches to the safety recovery policy, which manages safety-critical events to ensure the feasibility of humanoid control (see Section 4.2). To dynamically identify the "sweet spot" for policy switching or activation, we introduce a high-level policy that coordinates the low-level policies by utilizing historical observations and the robot's current status (see Section 4.3). Figure 1 illustrates the training pipeline of our HWC-LoCo.

4.1. Learning Goal-Tracking Policy for Efficient Humanoid Locomotion

The goal-tracking policy primarily focuses on tracking the provided command within the learning environment efficiently and naturally. This is achieved by optimizing the following objective function:

$$\max_{\pi_1} \mathbb{E}_{\rho_M^{\pi_1}} \left[\sum_{t=0}^{\infty} \gamma^t r_{\mathcal{T}}(s_t, a_t) \right] \text{ s.t. } \mathcal{D}_f(\rho_M^{\pi^E} \parallel \rho_M^{\pi_1}) \leq \epsilon_f \quad (5)$$

Note that compared to the complete objective (4), this goal-tracking objective focuses only on maximizing performance in the training environments' dynamics $P_{\mathcal{T}}^L$. Within this objective, the scale of the cumulative task rewards, $\sum_{t=0}^{\infty} \gamma^t r_{\mathcal{T}}$ reflects how effectively the policy π tracks locomotion-related commands, such as the robot's target linear and angular velocities. Appendix A.2 specifies the definition of our task reward.

In addition to the task rewards, a crucial aspect of the goal-tracking objective (5) is evaluating the distance between the occupancy measures of the trained policy and the expert policy. In the following, striving for concise representation, we represent $\rho_M^{\pi^E}$ and ρ_M^{π} by ρ^{π^E} and ρ^{π} . Driven by information theory, previous works (Hussein et al., 2017) primarily implement \mathcal{D}_f using metrics such as Kullback-Leibler (KL) divergence or Jensen-Shannon (JS) divergence. However, these metrics fail when the support of ρ^{π^E} and ρ^{π} has limited or zero overlap. In this study, we consider implement \mathcal{D}_f with Wasserstein-1 distance under the Kantorovich-Rubinstein duality (Villani et al., 2009) such that:

$$\mathcal{D}_f(\rho^{\pi^E} \parallel \rho^{\pi_1}) = \sup_{\|f_d\|_L \leq 1} \mathbb{E}_{x \sim \rho^{\pi^E}} [f_d(x)] - \mathbb{E}_{x \sim \rho^{\pi_1}} [f_d(x)] \quad (6)$$

where the bounded Lipschitz-norm $\|f_d\|_L \leq 1$ ensure the smoothness of functions f_d . Inspired by adversarial imitation learning (Ho & Ermon, 2016; Zhang et al., 2020), an effective and intuitive implementation of f_d is a discriminator for measuring whether x is generated by human experts, such that $f_d : \mathcal{X} \rightarrow \{0, 1\}$. This discriminator can be

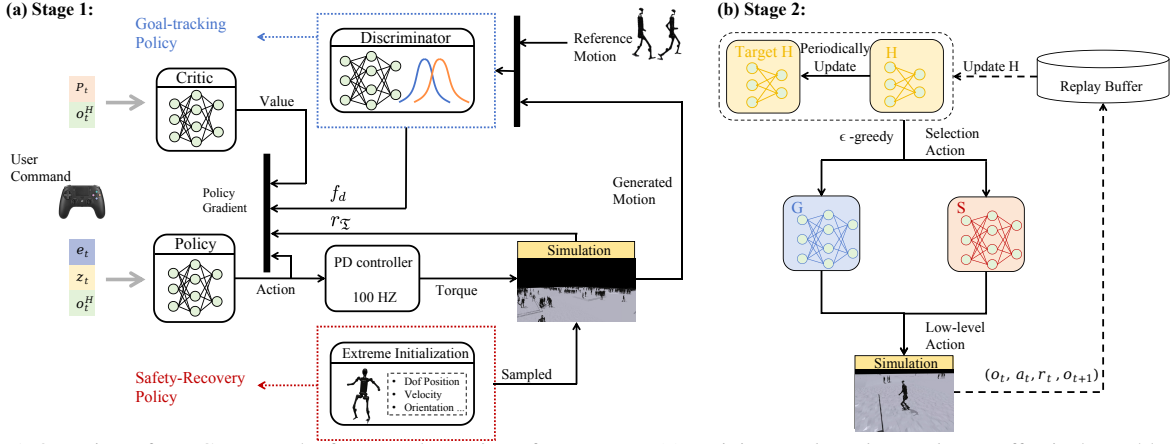


Figure 1. Overview of HWC-Loco: The framework consists of two stages: (a) Training *goal-tracking policy* to effectively enable human-like locomotion across diverse terrains (Section 4.1) and *safety recovery policy* to recover from safety-critical states (i.e., extreme-case) (Section 4.2). (b) Training the *high-level planning policy* to select between the two pre-trained low-level policies (Section 4.3), thereby ensuring locomotion stability and consistency.

learned by maximizing the following objective:

$$\max_{f_d} \mathbb{E}_{x \sim \rho^{\pi^E}} [f_d(x)] - \mathbb{E}_{x \sim \rho^{\pi_1}} [f_d(x)] + \beta \cdot \mathbb{E}_{\hat{x} \sim [\rho^{\pi^E}, \rho^{\pi_1}]} [(\|\nabla_{\hat{x}} f_d(\hat{x})\|_2 - 1)^2] \quad (7)$$

where weighted by β , the gradient penalty term enforces the Lipschitz continuity required by the Wasserstein distance (i.e., $\|f_d\|_L \leq 1$). During training, ρ^{π^E} represents the density of expert demonstration dataset \mathcal{D}^E , which is built from the CMU MoCap dataset (cmu). Additionally, we include data about humans standing, walking and running, enabling the robot to learn various human behaviors. We then retarget the motion data into a humanoid robot-compatible format, which we use as the training dataset.

Based on the discriminator, we can simplify the goal-tracking objective (5) by substituting \mathcal{D}_f with equation (6):

$$\max_{\pi_1} \mathbb{E}_{\rho^{\pi_1}} \left[\sum_{t=0}^{\infty} \gamma^t r_{\Sigma}(s_t, a_t) \right] \quad \text{s.t.} \quad \mathbb{E}_{\rho^{\pi^E}} [f_d(s^d)] - \mathbb{E}_{\rho^{\pi_1}} [f_d(s^d)] \leq \epsilon_f \quad (8)$$

where s^d is the input of the discriminator which is slight different from state s . Details can be seen in Appendix A.6.

Given that this format of the constrained RL problem has a zero duality gap (Paternain et al., 2019), we can transform it into an unconstrained objective by analyzing the Lagrange dual form of the original constrained RL problem:

$$\max_{\pi_1} \mathbb{E}_{\rho^{\pi_1}} \left[\sum_{t=0}^{\infty} \gamma^t [r_{\Sigma}(s_t, a_t) - \lambda f_d(s^d)] \right] \quad (9)$$

where λ denotes the optimal Lagrange multiplier. In practical implementation, the policy π and discriminator f_d can intuitively represent the generator and the discriminator

under the adversarial learning framework. In implementation, we utilize the proximal policy optimization algorithm (Schulman et al., 2017) to update the goal-tracking policy. By alternatively updating (7) and (9), we can develop a goal-tracking policy that effectively maximizes task rewards while closely mimicking the expert’s behavior.

4.2. Learning Safety Recovery Policy for Handling Safe-Critical Events

Our safety recovery policy primarily focuses on handling emergency events, thereby recovering the robot from safety-critical situations and preventing failures of locomotion tasks, such as loss of balance or control policy malfunctions. To learn the safety-recover policy, we mainly study the complete objective (4). Similarly, as it is introduced in Section 4.1, we implement the divergence metric \mathcal{D}_f with Wasserstein-1 distance, deriving the following objective:

$$\max_{\pi_2} \min_{\widehat{P}_{\tau} \in \mathfrak{P}_{\alpha}^L} \mathbb{E}_{\mu_0, \widehat{P}_{\tau}, \pi_2} \left[\sum_{t=0}^{\infty} \gamma^t r_{\Sigma}(s_t, a_t) - \lambda f_d(s_t, a_t) \right] \quad \text{s.t.} \quad \mathbb{E}_{\tau \sim (\mu_0, \widehat{P}_{\tau}, \pi_2)} [\phi(\tau)] \geq \epsilon_{\phi} \quad (10)$$

where ϵ_{ϕ} is a hyper-parameter. By comparing this objective with the goal-tracking objective (9), both consider task rewards and human mimicking performance. Despite the similarity, key differences lie in the incorporation of uncertainty in environmental dynamics and feasibility constraints in policy updates. These additions necessitate the construction of an extreme-case uncertainty set and the modeling of safety constraints by learning the feasibility function $\phi(\cdot)$.

Extreme-case Uncertainty Set. As in real-world deployment, there may have some complex terrains, external disturbances, hardware malfunctions, sensor noise, and errors caused by battery energy consumption. Those indicators may lead to extreme cases like falling and unexpected behavior. To model real-world extreme scenarios in the simula-

tion (i.e., modelling $\widehat{P_T}s$). We: 1) apply multi-scale external forces and torques to the humanoid body, 2) introduce random, high-intensity noise to the proprioceptive information and PD gains, 3) resample velocity commands to simulate malicious velocity inputs (Shi et al., 2024) within the goal-tracking policy, and 4) apply domain randomization to the training environment. Together, these dynamic variations construct the uncertainty set \mathfrak{P}_α^L , under which we learn the safety-recover policy. Details of our implementation are provided in Appendix A.4.

Zero-Moment Point (ZMP) Constraint. In the research of model-based robot control, a bipedal robot can be simplified to a linear inverted pendulum (Morisawa et al., 2006; Harada et al., 2006), where ZMP refers to the point where the ground reaction force has no horizontal moment. If the ZMP exits the support polygon (typically the foot’s contact area), the robot will quickly lose balance (Wieber, 2006; Feng et al., 2016; Scianca et al., 2020). Assuming a rigid body, stability is governed by gravity and the Center of Mass (CoM) accelerations, which also account for disturbances like obstacles and slippery surfaces. Under this assumption, ZMP is computed as follows:

$$\mathbf{p}_{\text{ZMP}}(s, a) = \mathbf{p}_{\text{CoM}}(s, a) - \frac{z_{\text{CoM}}(s, a)}{g} \cdot \ddot{\mathbf{p}}_{\text{CoM}}(s, a) \quad (11)$$

where 1) the vector \mathbf{p}_{CoM} denotes the x and y -coordinates of CoM position. 2) z_{CoM} is the height of the CoM. 3) g represents the acceleration due to gravity. 4) $\ddot{\mathbf{p}}_{\text{CoM}}$ indicates the accelerations of the CoM in the x and y -directions, calculated from the current and previous velocities. By leveraging the property of ZMP constraints, we implement the feasibility indicator in the safety recovery objective (10) as follows:

$$\phi(s, a) = \|\mathbf{p}_{\text{ZMP}}(s, a) - \mathbf{p}_{\text{ac}}\|_2 \quad (12)$$

where \mathbf{p}_{ac} represents the center of the support polygon (specific to each robot and known in advance). Intuitively, ϕ provides real-time insights into the robot’s stability and varies in its representation depending on the current support phase. Therefore, the humanoid robot can assess its stability in real time and use whole-body coordination to satisfy the ZMP constraint.

4.3. High-Level Planning for Policy Transition

The aforementioned low-level policies can achieve varying levels of optimality. A fundamental challenge is coordinating these policies to ensure that a humanoid robot can efficiently complete tasks while adhering to safety and robustness requirements. To address this challenge, we introduce a high-level planning policy that dynamically determines which policy to activate based on the specific state of humanoid robots. Considering the task of policy selection has a discrete action space, we utilize Double-DQN

(Van Hasselt et al., 2016) to learn this high-level policy π_0 based on the following objective:

$$\max_{\pi_0} \mathbb{E} \left[\sum_{t=0}^{\infty} \gamma^t [r_{\mathfrak{T}}(s_t, \bar{a}_t) - \mathbb{1}(\bar{a}_{t-1} \neq \bar{a}_t) - \alpha \mathbb{1}(s_t)] \right] \quad (13)$$

where 1) the policy selection action $\bar{a}_t \in \{0, 1\}^2$ denotes a one-hot vector featuring whether the goal-tracking policy π_1 and safety-recovery policy π_2 , 2) $\mathbb{1}(\bar{a}_{t-1} \neq \bar{a}_t)$ denotes the continuity identifier for discouraging the over-frequent switch of policies, and 3) $\mathbb{1}(s_t)$ denotes the termination identifier for preventing the failing of locomotion tasks. (2) and (3) are both $r_{\mathfrak{P}}$ defined in Section 3. More importantly, within this objective, by adjusting α , practitioners can adjust the trade-off safety guarantee and task completion. Details of training process and Algorithm Pseudocode can be found in Appendix A.2.

Practical Deployment. The training of humanoid control policy commonly relies on the privileged information \mathbb{P}_t , such as external disturbances, terrain dynamics, etc. We follow (Nahrendra et al., 2023) and infer \mathbb{P}_t by training a VAE-based estimator $P(e_t, z_t | o_t^H)$ where z_t captures the contextual embedding of the \mathbb{P}_t , and e_t consists of body velocity and ZMP features. To enhance the representation of $\phi(\cdot)$, we introduce frequency encoding, similar to the approach in (Mildenhall et al., 2021), to capture the subtle variations in $\phi(\cdot)$ for the policy. Additionally, instead of the zero-mean Gaussian prior, we introduce a learnable prior similar to (Luo et al., 2023). This learnable prior allows the encoder to dynamically adjust the distribution based on the observations, facilitating a more effective representation of environmental features in the latent space. Moreover, we include a certain degree of domain randomization in the learning of HWC-LoCo policies. The details of domain randomization are in Appendix A.4.

5. Experiment

Experiment Settings. To conduct a comprehensive evaluation, we quantify the control performance of HWC-LoCo in simulated (Issac Gym (Makoviychuk et al., 2021)) and realistic environments from the following perspectives: 1) *Scalability*: How effectively does HWC-LoCo navigate across diverse terrains and adapt to different embodiments? 2) *Robustness*: How well can HWC-LoCo stabilize the humanoid robot under varying levels of disturbance? 3) *Naturalness*: How effectively does HWC-LoCo imitate human-like movement norms? 4) *Sensitivity*: How promptly can the high-level planning policy activate the appropriate action policy?

Within these experiments, our evaluation metric includes a) *Success Rate*: The proportion of successful navigation across different scenarios. (Cui et al., 2024) b) *Goal Tracking performance*: The ability to accurately follow velocity commands by maximizing task rewards $r_{\mathfrak{T}}$ detailed in Appendix A.2 (Chen et al., 2024). c) *Human-Like behavior*:

Measured as the mean squared error (MSE) between the robot’s motions and sampled human motions.

Comparison Methods. To evaluate the effectiveness of different components in HWC-LoCo, we design a comparison method using an ablation approach as follows: 1) *HWC-LoCo-l* sets α to a lower value, thereby reducing the sensitivity of the high-level policy to failure events. 2) *Goal-Tracking Policy* removes the safety recovery mechanism and relies solely on the goal-tracking policy π_1 (Section 4.1). 3) *DreamWaQ-Humanoid* further removes the human imitation objective \mathcal{D}_f from objective (5), effectively reducing our method to an adaptation of DreamWaQ (Nahrendra et al., 2023) for humanoid control. 4) To highlight the benefits of our hierarchical policy, we compare a recent advancement of DreamWaQ, called *AHL* (Cui et al., 2024), which employs two-phase training for updating the locomotion policy.

5.1. Scalability: Locomotion across Diverse Terrains

We evaluate humanoid control policies across diverse terrains, including flat ground, obstacles, slopes, and stairs, ensuring comprehensive testing. To enable detailed comparisons, evaluations are conducted under both low-speed and high-speed commands. Specifically, low-speed commands are sampled as $v_x^c \sim [0.0, 1.0]$, $v_y^c \sim [-0.3, 0.3]$, and $w_z \sim [-0.5, 0.5]$, while high-speed commands follow $v_x^c \sim [1.0, 2.0]$, $v_y^c \sim [-0.6, 0.6]$, and $w_z^c \sim [-1.0, 1.0]$. Here, v_x^c , v_y^c , and w_z represent the commanded linear velocities along the x- and y-axes and angular velocity around the z-axis, respectively.

Table 2 shows that our HWC-LoCo achieves the highest success rate across all types of terrain while maintaining promising goal tracking and human mimic performance, demonstrating its exceptional robustness and reliability in the locomotion tasks. Specifically, as the complexity of the terrain increases (from flat surfaces to obstacles, slopes, and stairs), the advantage of our HWC-LoCo method in terms of success rate becomes increasingly apparent. Notably, in the high-speed stair terrain setting, HWC-LoCo has a significant higher success rate than all other policies, although its goal-tracking ability slightly decreases. This indicates that the policy prioritizes stability over aggressive goal pursuit. For example, when given a high-speed command, HWC-LoCo enables the policy to adapt dynamically in safety-critical situations (e.g., navigating stairs mid-air) rather than rigidly maintaining high velocity. Comparably, when downplaying the sensitivity to safe-critical events and removing the safety-recovery policy, the success data drop significantly from nearly 90% to around 60% on the testing environment with stairs and high-speed commands.

Cross Embodiment Validation. We apply HWC-LoCo to the Unitree G1 humanoid robot to validate its generalization capability. The testing terrains include all four previously mentioned types, and commands are sampled across the

full operational range. The results in Table 1 demonstrate differences between the G1 and H1 across three key metrics.

Table 1. Comparison of Embodiments

	Success Rate \uparrow	Goal Tracking \uparrow	Human-like \downarrow
Unitree H1	97.13 \pm 0.43	1.10 \pm 0.00	1.42 \pm 0.01
Unitree G1	98.14 \pm 0.35	1.12 \pm 0.01	1.02 \pm 0.02

5.2. Robustness: Stable Control under Disturbances

We conduct an extensive study on the robustness of HWC-LoCo under both simulated and realistic environments.

Robustness under Simulated Disturbance. We evaluated the ability of different methods to resist external impulse disturbances by continuously maintaining a standing posture. The external disturbances include forward forces, backward forces, lateral forces, and spinning torques. As shown in Table 3, HWC-LoCo demonstrates exceptional stability, effectively handling both forward and backward forces, with success rates approaching 100%. In response to lateral forces and spinning torques, HWC-LoCo also outperforms other policies. Compared to the goal-tracking only policy, these improvements suggest it requires an additional safety recovery policy to regain stability under disturbances.

Robustness in Realistic Deployment. We deploy the HWC-LoCo policy on a real humanoid robot and evaluate its performance under various external force disturbances. Specifically, the robot is subjected to continuous interference, including pushing and pulling its arms, kicking its legs, heavier kicks from both the front and back, and the application of rotational torque. Figure 8 (see Appendix B) illustrates the policy-switching process, along with the corresponding changes in the robot’s roll and pitch angles. When encountering external forces, the robot quickly transitions to a recovery policy, adjusting its posture and gait to restore stability. Notably, the policy does not rely solely on the recovery mechanism; instead, it seamlessly switches between the two policies. This behavior highlights the high-level policy’s ability to balance the trade-off between goal tracking and safety recovery.

5.3. Naturalness: Imitating Human-like Movements

In this experiment, we evaluate the robot’s ability to imitate human behavior by adapting its movements in response to varying velocity commands, ranging from low to high values. Figure 7 (see Appendix B) presents the results. When the velocity command is set to 0 m/s, the robot remains stationary. At 1.0 m/s, the robot walks forward with a natural stride, keeping its elbows relatively straight while its arms swing in coordination with its gait. At 2.5 m/s, the robot transitions to running, taking longer strides and gradually bending its elbows, closely resembling human running behavior. As the speed increases, the robot’s stride lengthens, and its step frequency adjusts dynamically, closely mimicking typical human locomotion patterns. This behavior

Table 2. Model performance in simulated environments. All policies are trained using three random seeds and then evaluated in 1000 distinct environments. Each evaluation runs for 1200 steps, which is equivalent to 12 seconds of real clock time.

Method	Flat			Obstacles		
	Success Rate(%) \uparrow	Goal Tracking \uparrow	Human - like \downarrow	Success Rate(%) \uparrow	Goal Tracking \uparrow	Human - like \downarrow
(a) Low Speed						
DreamWaQ	98.92 \pm 0.16	1.26 \pm 0.01	1.50 \pm 0.04	94.41 \pm 0.18	1.25 \pm 0.02	1.50 \pm 0.04
AHL	99.88 \pm 0.10	1.31 \pm 0.02	1.42 \pm 0.03	98.82 \pm 0.14	1.30 \pm 0.01	1.42 \pm 0.03
Goal-tracking Policy	99.97 \pm 0.01	1.33 \pm 0.01	1.39 \pm 0.02	99.60 \pm 0.10	1.32 \pm 0.01	1.39 \pm 0.02
HWC-LoCo-l	100.00 \pm 0.00	1.32 \pm 0.01	1.40 \pm 0.02	100.00 \pm 0.00	1.32 \pm 0.01	1.39 \pm 0.02
HWC-LoCo	100.00 \pm 0.00	1.28 \pm 0.01	1.41 \pm 0.03	100.00 \pm 0.00	1.28 \pm 0.01	1.40 \pm 0.02
(b) High Speed						
DreamWaQ	94.38 \pm 0.21	1.09 \pm 0.01	1.53 \pm 0.08	92.21 \pm 0.38	1.08 \pm 0.01	1.54 \pm 0.09
AHL	99.78 \pm 0.09	1.13 \pm 0.03	1.43 \pm 0.03	98.38 \pm 0.11	1.12 \pm 0.01	1.43 \pm 0.04
Goal-tracking Policy	99.95 \pm 0.04	1.14 \pm 0.00	1.40 \pm 0.03	99.20 \pm 0.15	1.13 \pm 0.01	1.42 \pm 0.02
HWC-LoCo-l	100.0 \pm 0.00	1.14 \pm 0.02	1.41 \pm 0.02	99.72 \pm 0.12	1.12 \pm 0.03	1.41 \pm 0.03
HWC-LoCo	100.0 \pm 0.00	1.13 \pm 0.02	1.41 \pm 0.03	99.92 \pm 0.06	1.12 \pm 0.02	1.42 \pm 0.02
Method	Slops			Stairs		
	Success Rate(%) \uparrow	Goal Tracking \uparrow	Human - like \downarrow	Success Rate(%) \uparrow	Goal Tracking \uparrow	Human - like \downarrow
(a) Low Speed						
DreamWaQ	92.31 \pm 0.40	1.19 \pm 0.02	1.52 \pm 0.08	74.32 \pm 1.30	1.19 \pm 0.03	1.56 \pm 0.09
AHL	98.83 \pm 0.15	1.21 \pm 0.01	1.42 \pm 0.03	93.73 \pm 0.70	1.21 \pm 0.04	1.42 \pm 0.01
Goal-tracking Policy	99.90 \pm 0.04	1.31 \pm 0.00	1.40 \pm 0.02	96.60 \pm 0.14	1.31 \pm 0.00	1.40 \pm 0.02
HWC-LoCo-l	100.00 \pm 0.00	1.23 \pm 0.02	1.40 \pm 0.03	99.80 \pm 0.08	1.21 \pm 0.02	1.41 \pm 0.01
HWC-LoCo	100.00 \pm 0.00	1.22 \pm 0.02	1.41 \pm 0.06	99.98 \pm 0.01	1.19 \pm 0.03	1.41 \pm 0.03
(b) High Speed						
DreamWaQ	90.46 \pm 0.43	1.05 \pm 0.01	1.57 \pm 0.10	60.58 \pm 0.64	1.06 \pm 0.01	1.58 \pm 0.12
AHL	97.36 \pm 0.23	1.12 \pm 0.01	1.45 \pm 0.03	67.48 \pm 0.77	1.09 \pm 0.01	1.46 \pm 0.04
Goal-tracking Policy	98.51 \pm 0.45	1.13 \pm 0.00	1.41 \pm 0.03	72.60 \pm 0.97	1.11 \pm 0.00	1.43 \pm 0.07
HWC-LoCo-l	99.95 \pm 0.02	1.12 \pm 0.02	1.42 \pm 0.03	78.92 \pm 0.45	1.10 \pm 0.01	1.44 \pm 0.08
HWC-LoCo	100.0 \pm 0.00	1.14 \pm 0.02	1.42 \pm 0.04	88.72 \pm 0.42	0.99 \pm 0.03	1.45 \pm 0.03

Table 3. Stability retention rate under impulse disturbances.

	Front \uparrow	Back \uparrow	Side \uparrow	Spinning \uparrow
DreamWaQ	60.20 \pm 0.62	57.25 \pm 0.52	44.44 \pm 0.36	54.38 \pm 0.41
AHL	90.01 \pm 0.64	89.15 \pm 0.23	70.65 \pm 0.74	82.43 \pm 0.24
G.-t. Policy	94.97 \pm 0.54	95.15 \pm 0.34	77.32 \pm 0.64	88.99 \pm 0.14
HWC-LoCo-l	98.35 \pm 0.34	97.97 \pm 0.33	88.84 \pm 0.20	93.95 \pm 0.61
HWC-LoCo	99.13 \pm 0.14	99.40 \pm 0.30	97.90 \pm 0.19	96.64 \pm 0.52

contrasts with some existing approaches (Gu et al., 2024c;d; Cui et al., 2024; Zhang et al., 2024b), where the robot maintains a constant step frequency regardless of the velocity command. In those methods, even at 0 m/s, the robot performs in-place stepping (Zhang et al., 2024b; Cui et al., 2024), which not only appears unnatural but also interferes with tasks requiring stable footing, such as manipulation.

5.4. Sensitivity: Activating the Proper Policy

Sensitive Analysis. We track the averaged proportion of activating goal-tracking policy across 4096 training environments with three random seeds, setting α to 0, 20, 50, and 200. Figure 2 shows the results. For $\alpha = 0, 20, 50$, the goal-tracking policy π_1 remains dominant, with the recovery policy π_2 activating only in extreme cases. However, at $\alpha = 200$, training becomes unstable due to sparse termination rewards, causing the recovery policy to be overlooked

and leading to overly conservative behavior.

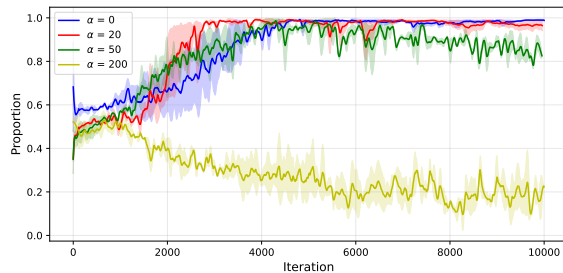


Figure 2. Averaged proportion of goal-tracking policy.

Parkour Test. Figure 9 shows the robot navigates multi-terrain (15cm steps, 20° slopes, wooden boards) at 0.3 m/s without external sensing. Upon encountering challenging terrain, it prioritizes safety by activating a recovery policy instead of persisting with goal tracking. Once it stabilizes on the terrain, it switches back to the goal-tracking policy, demonstrating adaptive control for dynamic environments.

6. Conclusion

We introduce HWC-LoCo, a hierarchical control framework for humanoid robots that incorporates an embedded safety recovery mechanism. This framework has been validated across various locomotion tasks, demonstrating exceptional scalability, robustness, naturalness, and adaptability across diverse tasks and scenarios. Notably, the safety mechanism

in HWC-LoCo extends beyond locomotion, enabling reliable performance in complex tasks through a dynamic task-safety balance. This ensures robust operation in real-world deployments, positioning HWC-LoCo as a foundational solution for safety-critical applications such as industrial automation and assistive robotics. A promising direction for future research is integrating HWC-LoCo with upper-body manipulation skills, enabling safety-critical control across a broader range of tasks involving different objects.

Impact Statement

The broader impact of this work lies in its potential to significantly enhance the capabilities of humanoid robots, enabling them to perform complex locomotion tasks safely and effectively across diverse and unpredictable environments.

From an ethical perspective, the development of humanoid robots with advanced locomotion capabilities raises important questions about safety, accountability, and the potential societal implications of widespread adoption. While HWC-LoCo prioritizes safety through its robust control mechanisms, ensuring these systems consistently operate within ethical and safety norms is critical to preventing harm, particularly in environments shared with humans. Additionally, as humanoid robots become more capable of replacing human roles in workplaces, concerns about job displacement, economic inequality, and the societal impact of automation must be addressed. Proactive measures, such as workforce reskilling, equitable distribution of benefits, and collaboration between policymakers and researchers, will be necessary to mitigate these risks.

In the long term, HWC-LoCo has the potential to significantly improve societal well-being. Humanoid robots equipped with robust locomotion algorithms could assist in tasks that are dangerous or physically demanding for humans, such as search-and-rescue missions, caregiving for the elderly or disabled, and operating in hazardous industrial environments. However, the deployment of such robots must be guided by principles of transparency, fairness, and inclusivity to ensure they serve societal needs without reinforcing biases or creating unintended harms.

References

- CMU, Cmu graphics lab motion capture database, <http://mocap.cs.cmu.edu/>.
- Chen, S., Zhang, B., Mueller, M. W., Rai, A., and Sreenath, K. Learning torque control for quadrupedal locomotion. In *2023 IEEE-RAS 22nd International Conference on Humanoid Robots (Humanoids)*, pp. 1–8. IEEE, 2023.
- Chen, Z., He, X., Wang, Y.-J., Liao, Q., Ze, Y., Li, Z., Sastry, S. S., Wu, J., Sreenath, K., Gupta, S., et al. Learning smooth humanoid locomotion through lipschitz-constrained policies. *arXiv preprint arXiv:2410.11825*, 2024.
- Cheng, X., Ji, Y., Chen, J., Yang, R., Yang, G., and Wang, X. Expressive whole-body control for humanoid robots. *arXiv preprint arXiv:2402.16796*, 2024.
- Chignoli, M., Kim, D., Stanger-Jones, E., and Kim, S. The mit humanoid robot: Design, motion planning, and control for acrobatic behaviors. In *2020 IEEE-RAS 20th International Conference on Humanoid Robots (Humanoids)*, pp. 1–8. IEEE, 2021.
- Cui, W., Li, S., Huang, H., Qin, B., Zhang, T., Zheng, L., Tang, Z., Hu, C., Yan, N., Chen, J., et al. Adapting humanoid locomotion over challenging terrain via two-phase training. In *8th Annual Conference on Robot Learning*, 2024.
- Duan, H., Pandit, B., Gadde, M. S., Van Marum, B., Dao, J., Kim, C., and Fern, A. Learning vision-based bipedal locomotion for challenging terrain. In *2024 IEEE International Conference on Robotics and Automation (ICRA)*, pp. 56–62. IEEE, 2024.
- Feng, S., Xinjilefu, X., Atkeson, C. G., and Kim, J. Robust dynamic walking using online foot step optimization. In *2016 IEEE/RSJ International Conference on Intelligent Robots and Systems (IROS)*, pp. 5373–5378. IEEE, 2016.
- Fu, Z., Zhao, Q., Wu, Q., Wetzstein, G., and Finn, C. Humanplus: Humanoid shadowing and imitation from humans. In *8th Annual Conference on Robot Learning*, 2024.
- Gouaillier, D., Hugel, V., Blazevic, P., Kilner, C., Monceaux, J., Lafourcade, P., Marnier, B., Serre, J., and Maisonnier, B. Mechatronic design of NAO humanoid. In *IEEE International Conference on Robotics and Automation, ICRA*, pp. 769–774, 2009.
- Gu, S., Yang, L., Du, Y., Chen, G., Walter, F., Wang, J., and Knoll, A. A review of safe reinforcement learning: Methods, theories, and applications. *IEEE Transactions on Pattern Analysis and Machine Intelligence*, 46(12): 11216–11235, 2024a.
- Gu, X., Wang, Y., Zhu, X., Shi, C., Guo, Y., Liu, Y., and Chen, J. Advancing humanoid locomotion: Mastering challenging terrains with denoising world model learning. *arXiv preprint arXiv:2408.14472*, 2024b.
- Gu, X., Wang, Y.-J., and Chen, J. Humanoid-gym: Reinforcement learning for humanoid robot with zero-shot sim2real transfer. *arXiv preprint arXiv:2404.05695*, 2024c.

- Gu, X., Wang, Y.-J., Zhu, X., Shi, C., Guo, Y., Liu, Y., and Chen, J. Advancing humanoid locomotion: Mastering challenging terrains with denoising world model learning. *arXiv preprint arXiv:2408.14472*, 2024d.
- Harada, K., Kajita, S., Kaneko, K., and Hirukawa, H. An analytical method for real-time gait planning for humanoid robots. *International Journal of Humanoid Robotics*, 3 (01):1–19, 2006.
- He, T., Luo, Z., He, X., Xiao, W., Zhang, C., Zhang, W., Kitani, K., Liu, C., and Shi, G. Omnih2o: Universal and dexterous human-to-humanoid whole-body teleoperation and learning. *arXiv preprint arXiv:2406.08858*, 2024a.
- He, T., Luo, Z., Xiao, W., Zhang, C., Kitani, K., Liu, C., and Shi, G. Learning human-to-humanoid real-time whole-body teleoperation. *arXiv preprint arXiv:2403.04436*, 2024b.
- He, T., Xiao, W., Lin, T., Luo, Z., Xu, Z., Jiang, Z., Kautz, J., Liu, C., Shi, G., Wang, X., Fan, L., and Zhu, Y. HOVER: versatile neural whole-body controller for humanoid robots. *arXiv preprint arXiv:2410.21229*, 2024c.
- He, T., Zhang, C., Xiao, W., He, G., Liu, C., and Shi, G. Agile but safe: Learning collision-free high-speed legged locomotion. *arXiv preprint arXiv:2401.17583*, 2024d.
- Ho, J. and Ermon, S. Generative adversarial imitation learning. In Lee, D. D., Sugiyama, M., von Luxburg, U., Guyon, I., and Garnett, R. (eds.), *Advances in Neural Information Processing Systems, NeurIPS*, pp. 4565–4573, 2016.
- Hussein, A., Gaber, M. M., Elyan, E., and Jayne, C. Imitation learning: A survey of learning methods. *ACM Computing Surveys*, 50(2):21:1–21:35, 2017.
- Kim, D., Kwon, H., Kim, J., Lee, G., and Oh, S. Stage-wise reward shaping for acrobatic robots: A constrained multi-objective reinforcement learning approach. *arXiv preprint arXiv:2409.15755*, 2024.
- Kumar, A., Li, Z., Zeng, J., Pathak, D., Sreenath, K., and Malik, J. Adapting rapid motor adaptation for bipedal robots. In *2022 IEEE/RSJ International Conference on Intelligent Robots and Systems (IROS)*, pp. 1161–1168. IEEE, 2022.
- Lai, H., Zhang, W., He, X., Yu, C., Tian, Z., Yu, Y., and Wang, J. Sim-to-real transfer for quadrupedal locomotion via terrain transformer. In *2023 IEEE International Conference on Robotics and Automation (ICRA)*, pp. 5141–5147. IEEE, 2023.
- Li, Z., Cheng, X., Peng, X. B., Abbeel, P., Levine, S., Berseth, G., and Sreenath, K. Reinforcement learning for robust parameterized locomotion control of bipedal robots. In *2021 IEEE International Conference on Robotics and Automation (ICRA)*, pp. 2811–2817. IEEE, 2021.
- Li, Z., Peng, X. B., Abbeel, P., Levine, S., Berseth, G., and Sreenath, K. Robust and versatile bipedal jumping control through reinforcement learning. *arXiv preprint arXiv:2302.09450*, 2023.
- Long, J., Ren, J., Shi, M., Wang, Z., Huang, T., Luo, P., and Pang, J. Learning humanoid locomotion with perceptive internal model. *arXiv preprint arXiv:2411.14386*, 2024.
- Luo, Z., Cao, J., Merel, J., Winkler, A., Huang, J., Kitani, K., and Xu, W. Universal humanoid motion representations for physics-based control. *arXiv preprint arXiv:2310.04582*, 2023.
- Mahmood, N., Ghorbani, N., Troje, N. F., Pons-Moll, G., and Black, M. J. AMASS: archive of motion capture as surface shapes. In *IEEE/CVF International Conference on Computer Vision, ICCV*, pp. 5441–5450. IEEE, 2019.
- Makoviychuk, V., Wawrzyniak, L., Guo, Y., Lu, M., Storey, K., Macklin, M., Hoeller, D., Rudin, N., Allshire, A., Handa, A., et al. Isaac gym: High performance gpu-based physics simulation for robot learning. *arXiv preprint arXiv:2108.10470*, 2021.
- Margolis, G. B. and Agrawal, P. Walk these ways: Tuning robot control for generalization with multiplicity of behavior. In *Conference on Robot Learning*, pp. 22–31. PMLR, 2023.
- Mildenhall, B., Srinivasan, P. P., Tancik, M., Barron, J. T., Ramamoorthi, R., and Ng, R. Nerf: Representing scenes as neural radiance fields for view synthesis. *Communications of the ACM*, 65(1):99–106, 2021.
- Moos, J., Hansel, K., Abdulsamad, H., Stark, S., Clever, D., and Peters, J. Robust reinforcement learning: A review of foundations and recent advances. *Machine Learning and Knowledge Extraction*, pp. 276–315, 2022.
- Morisawa, M., Harada, K., Kajita, S., Kaneko, K., Kanehiro, F., Fujiwara, K., Nakaoka, S., and Hirukawa, H. A biped pattern generation allowing immediate modification of foot placement in real-time. In *2006 6th IEEE-RAS International Conference on Humanoid Robots*, pp. 581–586. IEEE, 2006.
- Nahrendra, I. M. A., Yu, B., and Myung, H. Dreamwaq: Learning robust quadrupedal locomotion with implicit terrain imagination via deep reinforcement learning. In *2023 IEEE International Conference on Robotics and Automation (ICRA)*, pp. 5078–5084. IEEE, 2023.

- Nasiriany, S., Maddukuri, A., Zhang, L., Parikh, A., Lo, A., Joshi, A., Mandlekar, A., and Zhu, Y. Robocasa: Large-scale simulation of everyday tasks for generalist robots. *arXiv preprint arXiv:2406.02523*, 2024.
- Paolo, G., Gonzalez-Billandon, J., and Kégl, B. Position: A call for embodied AI. In *Forty-first International Conference on Machine Learning, ICML*, 2024.
- Paternain, S., Chamon, L. F. O., Calvo-Fullana, M., and Ribeiro, A. Constrained reinforcement learning has zero duality gap. In *Advances in Neural Information Processing Systems, NeurIPS*, pp. 7553–7563, 2019.
- Radford, N. A., Strawser, P., Hambuchen, K. A., Mehling, J. S., Verdeyen, W. K., Donnan, A. S., Holley, J., Sanchez, J., Nguyen, V., Bridgwater, L. B., Berka, R., Ambrose, R. O., Markee, M. M., Fraser-Chanpong, N. J., McQuin, C., Yamokoski, J. D., Hart, S., Guo, R., Parsons, A., Wightman, B., Dinh, P., Ames, B., Blakely, C., Edmondson, C., Sommers, B., Rea, R., Tobler, C., Bibby, H., Howard, B., Niu, L., Lee, A., Conover, M., Truong, L., Reed, R., Chesney, D., Jr., R. P., Johnson, G., Fok, C., Paine, N., Sentis, L., Cousineau, E. A., Sinnet, R. W., Lack, J., Powell, M. J., Morris, B., Ames, A. D., and Akinyode, J. Valkyrie: Nasa’s first bipedal humanoid robot. *Journal of Field Robotics*, 32(3):397–419, 2015.
- Radosavovic, I., Xiao, T., Zhang, B., Darrell, T., Malik, J., and Sreenath, K. Real-world humanoid locomotion with reinforcement learning. *Science Robotics*, 9(89): eadi9579, 2024.
- Rudin, N., Hoeller, D., Reist, P., and Hutter, M. Learning to walk in minutes using massively parallel deep reinforcement learning. In *Conference on Robot Learning*, pp. 91–100. PMLR, 2022.
- Saeedvand, S., Jafari, M., Aghdasi, H. S., and Baltes, J. A comprehensive survey on humanoid robot development. *Knowledge Engineering Review*, 34:e20, 2019.
- Sakagami, Y., Watanabe, R., Aoyama, C., Matsunaga, S., Higaki, N., and Fujimura, K. The intelligent ASIMO: system overview and integration. In *IEEE/RSJ International Conference on Intelligent Robots and Systems, IROS*, pp. 2478–2483. IEEE, 2002.
- Schulman, J., Wolski, F., Dhariwal, P., Radford, A., and Klimov, O. Proximal policy optimization algorithms. *arXiv preprint arXiv:1707.06347*, 2017.
- Scianca, N., De Simone, D., Lanari, L., and Oriolo, G. Mpc for humanoid gait generation: Stability and feasibility. *IEEE Transactions on Robotics*, 36(4):1171–1188, 2020.
- Sentis, L. and Khatib, O. A whole-body control framework for humanoids operating in human environments. In *IEEE International Conference on Robotics and Automation, ICRA*, pp. 2641–2648. IEEE, 2006.
- Sferrazza, C., Huang, D.-M., Lin, X., Lee, Y., and Abbeel, P. Humanoidbench: Simulated humanoid benchmark for whole-body locomotion and manipulation. *arXiv preprint arXiv:2403.10506*, 2024.
- Shi, F., Zhang, C., Miki, T., Lee, J., Hutter, M., and Coros, S. Rethinking robustness assessment: Adversarial attacks on learning-based quadrupedal locomotion controllers. *arXiv preprint arXiv:2405.12424*, 2024.
- Shi, H., Zhou, B., Zeng, H., Wang, F., Dong, Y., Li, J., Wang, K., Tian, H., and Meng, M. Q.-H. Reinforcement learning with evolutionary trajectory generator: A general approach for quadrupedal locomotion. *IEEE Robotics and Automation Letters*, 7(2):3085–3092, 2022.
- Tan, W., Fang, X., Zhang, W., Song, R., Chen, T., Zheng, Y., and Li, Y. A hierarchical framework for quadruped omnidirectional locomotion based on reinforcement learning. *IEEE Transactions on Automation Science and Engineering*, 2023.
- Tao, S., Xiang, F., Shukla, A., Qin, Y., Hinrichsen, X., Yuan, X., Bao, C., Lin, X., Liu, Y., Chan, T.-k., et al. Maniskill3: Gpu parallelized robotics simulation and rendering for generalizable embodied ai. *arXiv preprint arXiv:2410.00425*, 2024.
- Van Hasselt, H., Guez, A., and Silver, D. Deep reinforcement learning with double q-learning. In *Proceedings of the AAAI conference on artificial intelligence*, volume 30, 2016.
- Viano, L., Huang, Y., Kamalaruban, P., Innes, C., Ramamoorthy, S., and Weller, A. Robust learning from observation with model misspecification. In *International Conference on Autonomous Agents and Multiagent Systems*, pp. 1337–1345, 2022.
- Villani, C. et al. *Optimal transport: old and new*, volume 338. Springer, 2009.
- Wang, Z., Wei, W., Yu, R., Wu, J., and Zhu, Q. Toward understanding key estimation in learning robust humanoid locomotion. *arXiv preprint arXiv:2403.05868*, 2024.
- Wieber, P.-B. Trajectory free linear model predictive control for stable walking in the presence of strong perturbations. In *2006 6th IEEE-RAS International Conference on Humanoid Robots*, pp. 137–142. IEEE, 2006.
- Zhang, C., Xiao, W., He, T., and Shi, G. Wococo: Learning whole-body humanoid control with sequential contacts. In *Annual Conference on Robot Learning*, 2024a.

Zhang, Q., Cui, P., Yan, D., Sun, J., Duan, Y., Han, G., Zhao, W., Zhang, W., Guo, Y., Zhang, A., et al. Whole-body humanoid robot locomotion with human reference. In *2024 IEEE/RSJ International Conference on Intelligent Robots and Systems (IROS)*, pp. 11225–11231. IEEE, 2024b.

Zhang, X., Li, Y., Zhang, Z., and Zhang, Z. f-gail: Learning f-divergence for generative adversarial imitation learning. In *Advances in Neural Information Processing Systems, NeurIPS*, 2020.

Zhuang, Z., Fu, Z., Wang, J., Atkeson, C., Schwertfeger, S., Finn, C., and Zhao, H. Robot parkour learning. *arXiv preprint arXiv:2309.05665*, 2023.

Zhuang, Z., Yao, S., and Zhao, H. Humanoid parkour learning. In *8th Annual Conference on Robot Learning*, 2024.

A. Additional Training Details

A.1. Motion Retargeting

Our motion data is derived from the CMU Mocap dataset (cmu), which exclusively encompasses human locomotion data, featuring a diverse array of walking, jogging, and running styles. In aggregate, we have loaded 318 motion sequences, totaling 3729.18 seconds in duration. Our motion retargeting methodology closely follows the approach outlined in (Cheng et al., 2024). We have meticulously aligned the humanoid robot’s skeleton with that of humans, incorporating adjustments such as rotation, translation, and scaling. Additionally, we map human joints onto the humanoid robot’s structure. Specifically, the human motion data is adapted to the humanoid robot’s framework by mapping local information. Both the Unitree H1 and G1 robots possess shoulder and hip joints that are functionally equivalent to spherical joints. During the retargeting process, the three hip and shoulder joints are treated as a single spherical joint, corresponding to the human’s spherical joint. For one-dimensional joints such as the elbow and torso, the rotation angle is projected onto the corresponding rotation axis of the joint axes.

Table 4. Double-DQN Parameters

Parameter	Value
Batch Size	128
Learning Rate	1e-4
Gamma	0.99
Max Grad Norm	1.0
Replay Buffer Capacity	2000000
Switch Penalty Coefficient	0.001
Target Update Frequency	50
Optimizer	Adam
Loss Function	MSELoss
Initial Epsilon	0.1
Minimum Epsilon	0.001
Epsilon Decay Rate	0.999

Table 5. Network Structure

Layer	Details
Layer 1	[input_dim, 256]
Layer 2	Activation: ReLU
Layer 3	Regularization: Dropout
Layer 4	[256, 128]
Layer 5	[128, 64]
Layer 6	Activation: ReLU
Layer 7	[64, output_dim]

A.2. Implementation Details

Proprioception: For the Unitree H1, proprioception $\mathbf{o}_t^p \in \mathbb{R}^{65}$, which denotes the internal state of the robot, including the base angular velocity $\mathbf{w}_t \in \mathbb{R}^3$, base roll $\mathbf{r}_t \in \mathbb{R}^1$, base pitch $\mathbf{p}_t \in \mathbb{R}^1$, degrees of freedom (DOF) positions $\mathbf{q}_t \in \mathbb{R}^{19}$, DOF velocities $\dot{\mathbf{q}}_t \in \mathbb{R}^{19}$, previous actions $\mathbf{a}_{t-1} \in \mathbb{R}^{19}$, and projected gravity $\mathbf{g}_t \in \mathbb{R}^3$. The projected gravity refers to the component of gravity expressed in the robot’s local coordinate system. For the Unitree G1, proprioception $\mathbf{o}_t^p \in \mathbb{R}^{77}$, includes base angular velocity $\mathbf{w}_t \in \mathbb{R}^3$, base roll $\mathbf{r}_t \in \mathbb{R}^1$, base pitch $\mathbf{p}_t \in \mathbb{R}^1$, DOF positions $\mathbf{q}_t \in \mathbb{R}^{23}$, DOF velocities $\dot{\mathbf{q}}_t \in \mathbb{R}^{23}$, previous actions $\mathbf{a}_{t-1} \in \mathbb{R}^{23}$, and projected gravity $\mathbf{g}_t \in \mathbb{R}^3$. As with the H1, the projected gravity denotes the component of gravity in the robot’s local coordinate system.

Action Space: The policy outputs continuous actions $\mathbf{a}_t \in \mathbb{R}^n$, which are utilized as target positions for a PD controller to compute joint torques. The actions correspond to the robot’s actuated degrees of freedom: specifically, $\mathbf{a}_t \in \mathbb{R}^{19}$ (19 DoF) for the Unitree H1 and $\mathbf{a}_t \in \mathbb{R}^{23}$ (23 DoF) for the Unitree G1.

Terrain details: Terrains in the training environment simulated by Isaac Gym (Makoviychuk et al., 2021) include flats, obstacles, slopes, and stairs. An example of these terrains is shown in Figure 3.

Low-level Policy Training: For all the low-level policies training, the commands are sampled from ranges: $v_x^c \sim [-0.6, 2.5]$, $v_y^c \sim [-0.6, 0.6]$ and $w_z^c \sim [-1.0, 1.0]$. During the initial training of the humanoid robot on uneven terrain, the robot often remains stationary due to the high difficulty of navigating complex surfaces. To address this, we introduce a terrain curriculum method (Makoviychuk et al., 2021). The training terrain consists of various types, including flat planes, rough surfaces, steps, and slopes. As the robot achieves a goal-tracking performance of 70% of the commanded velocity, the terrain difficulty increases. Conversely, if the goal-tracking performance drops below 40% of the commanded velocity, the terrain becomes easier.

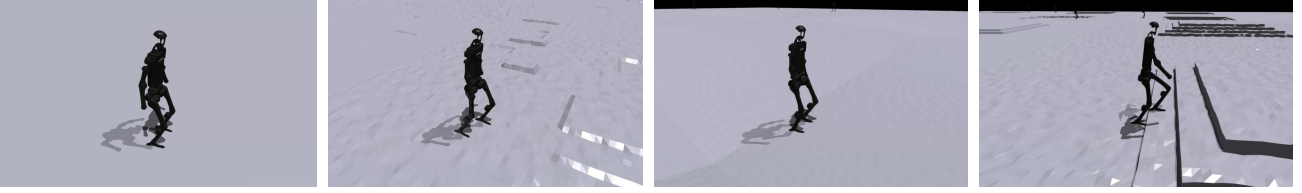


Figure 3. Visualization of different terrains. From left to right, the terrains are flats, obstacles, slopes, and stairs

Learning for Policy Transition: High-level planning policy is utilized to switch between low-level policies, ensuring compliance with robustness constraints. For the High-level policy, the input is the same set of observations as used by the low-level policies, with the output being a two-dimensional Q-value. During training, two trained low-level policies are loaded and rolled out to generate training data for optimizing the high-level policy. We train this high-level policy in the simulation environment mentioned detailed in Section 4.2, focusing on locomotion goals as the primary task. The objective is to enable the robot to track goal commands across a variety of terrains. The details of the training process is in Algorithm 1

Algorithm 1 Training for High-level Policy using Double-DQN

Input: Environment env , Selector network S , Target network S_{target} , Goal-tracking policy L , Recovery policy R
 Initialize: Learning rate α , Discount factor γ , Exploration rate ϵ , Replay buffer B , Target update frequency f_{target} , Switch penalty λ_{switch} , Exploration decay ϵ_{decay} , Minimum exploration ϵ_{min}
 $S_{target} \leftarrow S$ {Initialize target network}
repeat
 Observe initial state s from env
 Reset cumulative reward R_{total} , step count n , previous action $a_{prev} \leftarrow \text{None}$
 while not done **do**
 Compute $Q(s, \cdot) \leftarrow S(s)$, select action a with ϵ -greedy
 Compute switch penalty: $r_{penalty} \leftarrow \lambda_{switch} \cdot \mathbf{1}[a \neq a_{prev}]$
 Execute a , observe reward r , next state s' , and done signal d
 Store $(s, a, r + r_{penalty}, s', d)$ in B
 Update $s \leftarrow s'$, $a_{prev} \leftarrow a$
 $R_{total} \leftarrow R_{total} + r$, $n \leftarrow n + 1$
 if $B.size() \geq \text{batch size}$ **then**
 Sample (s, a, r, s', d) from B
 $a' \leftarrow \arg \max_{a'} S(s', a')$ {Online network selects action}
 $Q^{target}(s', a') \leftarrow S_{target}(s', a')$ {Target network evaluates}
 Compute target: $Q^{target}(s, a) \leftarrow r + \gamma(1 - d)Q^{target}(s', a')$
 Update S by minimizing: $\mathcal{L} = (S(s, a) - Q^{target}(s, a))^2$
 end if
 if $n \bmod f_{target} = 0$ **then**
 $S_{target} \leftarrow S$ {Sync target network}
 end if
 end while
 Decay exploration rate: $\epsilon \leftarrow \max(\epsilon \cdot \epsilon_{decay}, \epsilon_{min})$
until convergence criteria met
Output: Trained Selector Network S

Reward Details: To better facilitate efficient humanoid locomotion, our task reward is defined as (Gu et al., 2024c;d):

$$r_{\mathcal{T}} = \alpha_1 \exp\left(-\frac{\|v_{xy}^c - v_{xy}\|_2^2}{\sigma_{lin}^2}\right) + \alpha_2 \exp\left(-\frac{\|w_z^c - w_z\|_2^2}{\sigma_{ang}^2}\right)$$

where 1) v_{xy}^c denotes the commanded linear velocity along the x and y axes, while w_z^c is the commanded yaw velocity. 2)

v_{xy} and w_z represent the corresponding base velocities of the humanoid robot. 3) α_1 and α_2 indicate the hyperparameters that are utilized to adjust the importance of the different velocity terms. 4) σ_{lin}^2 and σ_{ang}^2 control the precision of the expected command tracking. Smaller values of σ_{lin}^2 and σ_{ang}^2 enhance the precision of command tracking for humanoid robots. However, they may hinder reward acquisition during the initial stages of training.

To enable the recovery policy to learn stable posture restoration and facilitate smooth policy transitions, we introduce a stand reward. It can be calculated as:

$$r_{\text{stand}} = \|\mathbf{q}_t - \mathbf{q}_{\text{default}}\|_2^2.$$

where $\mathbf{q}_{\text{default}}$ represents a default standing pose.

For safety realistic deployment, we add some energy and safety reward for the low-level policies training. These rewards are shown in Table.

Table 6. Safety & Energy Reward

Term	Expression	Weight
DoF position limits	$\mathbf{1}(\mathbf{q}_t \notin [\mathbf{q}_{\text{min}}, \mathbf{q}_{\text{max}}])$	$-1e^2$
DoF acceleration	$\ \ddot{\mathbf{q}}_t\ _2^2$	$-1e^{-7}$
DoF velocity	$\ \dot{\mathbf{q}}_t\ _2^2$	$-5e^{-4}$
Action rate	$\ \mathbf{a}_t - \mathbf{a}_{t-1}\ _2^2$	$-2e^{-3}$
Torque	$\ \tau_t\ $	$-1e^{-5}$
Collision	$\sum_{i \in \text{contact}} \mathbf{1}\{\ F_i\ > 1.0\}$	-10

A.3. Saliency Analysis of Observations

We adopt an integrated gradients method similar to (Wang et al., 2024) to assess the importance of different parts of the observation to the policy, as shown in Fig.4. For the recovery policy, ZMP encoding emerges as the most crucial element, followed by the estimated velocity as the second most important factor. Additionally, the robot’s current proprioception and historical proprioception are also significant, while environmental latent has only a slight influence. This is because, for the recovery policy, it is essential to satisfy the ZMP constraints to ensure the robot’s stability and safety. For the high-level policy, ZMP encoding is also the most important component, indicating that it provides vital information for the policy’s decision-making process, thereby enhancing its ability to perceive the robot’s stability. Furthermore, the environmental latent variable proves to be more important compared to the recovery policy, suggesting that environmental factors, such as changes in terrain, can influence the decision-making process.

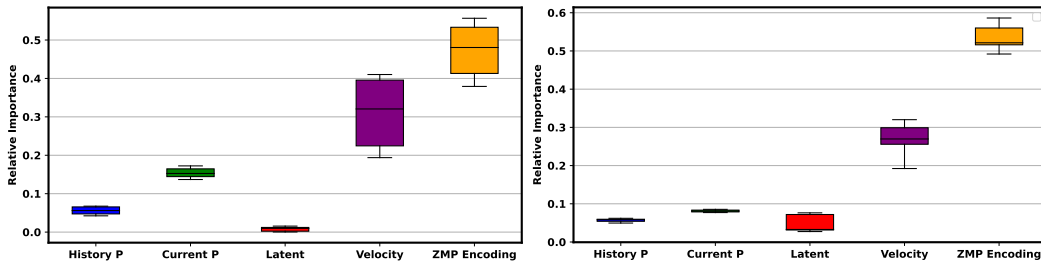


Figure 4. Importance of Observations

A.4. Extreme Initialization

To simulate extreme scenarios that may occur in real-world deployment, we identify three primary causes of such cases: external disturbances, hardware malfunctions, and malicious velocity inputs. Additionally, we retain domain randomization to enhance the generalization of physical dynamics within the simulation environment. The specific details are outlined as follows:

1) **External disturbances:** We apply external disturbances to every component of the robot. The external forces and torques

are applied along the x, y, and z axes, with each direction sampled from the range of -200 N to 200 N for forces and -200 Nm to 200 Nm for torques. These disturbance forces and torques are updated at a frequency of 1 Hz.

2) **Hardward magnification** : Random, high-intensity noise is introduced to the proprioceptive information and PD gains. The noise added to the proprioceptive data simulates sensor errors that may occur during real-world deployment. The noise applied to the PD gains simulates fluctuations in motor strength, reflecting potential issues in the robot’s actuators. The parameters for this noise are detailed in Table 7.

3) **Malicious velocity**: Velocity commands are resampled from the command range, with updates occurring at a frequency of 5 Hz. Notably, this resampling mechanism is activated once the terrain curriculum exceeds half of its total progression.

4) **Domain randomization**: Domain randomization is applied to all the training environments. This technique introduces variability in the environment’s parameters, such as friction and gravity. The specifics of the domain randomization are provided in Table 8.

To improve the generalization of recovery ability, we utilize random initialization with extreme case initialization. The parameters are shown in Table 9

Table 7. Proprioception Noise Parameters

Parameter	Range	Operator
DOF Position Noise	0.04	additive
DOF Velocity Noise	0.30	additive
Angular Velocity Noise	1.00	additive
IMU Noise	0.40	additive
Gravity Noise	0.10	additive
PD Gains	0.20	additive

Table 8. Domain Randomization Parameters

Parameter	Range	Operator
Friction	[0.6, 2.0]	additive
Base Mass	[-1.0, 5.0]	additive
Base CoM	[-0.07, 0.07]	additive
Motor Strength	[0.8, 1.2]	scaling
Action Delay	[0, 5]	-
Link Mass	[0.7, 1.3]	scaling
Gravity	[-0.1, 0.1]	additive

Table 9. Random Initialization Parameters

Parameter	Range
Linear Velocity (x)	[-1.0, 2.5]
Linear Velocity (y)	[-1.0, 1.0]
Linear Velocity (z)	[-0.4, 0.4]
Angular Velocity	[-1.0, 1.0]
DOF Position	[0.2 × default, 1.8 × default]
DOF Velocity	[-0.2, 0.2]
Pitch Angle	[-0.25, 0.25]
Yaw Angle	[-0.4, 0.4]
Position	[-2, 2]

Extreme-Case Analysis: We record nearly 60000 normal state data with randomly sampled commands in diverse terrain settings in 5. We record nearly 10000 extreme cases in the \mathfrak{P}_α^L . Some of the terminal states are visualized in Fig. 6. For the extreme states, the distribution of velocity is close to the command ranges. Roll pitch and their velocity are in a common range, which is near zeros. For the normal states, the distribution of linear velocity overlaps with the command velocity range, with a dense cluster around the high-velocity value of 2 m/s. Regarding yaw velocity, most values fall within the commanded range. However, there are instances of high speed, with some even approaching 10 m/s. This may be due to the robot’s extreme behaviors when encountering unseen situations influenced by external forces and random noise. Regarding the roll-pitch velocity, the pitch velocity shows a higher degree of fluctuation. Similarly, in the roll pitch distribution, for pitch, there is a concentrated distribution at a pitch of 1 m/s, which is one of the terminal conditions. These two figures suggest that the robot is tripped by obstacles during its motion and thus terminates, for instance, when it hits steps or gravel during high-speed motion.

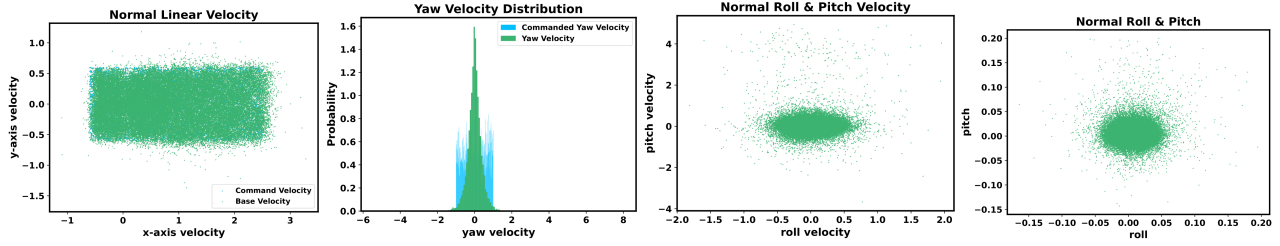


Figure 5. Normal State: Policy rollout’s state distribution in the original learning environment

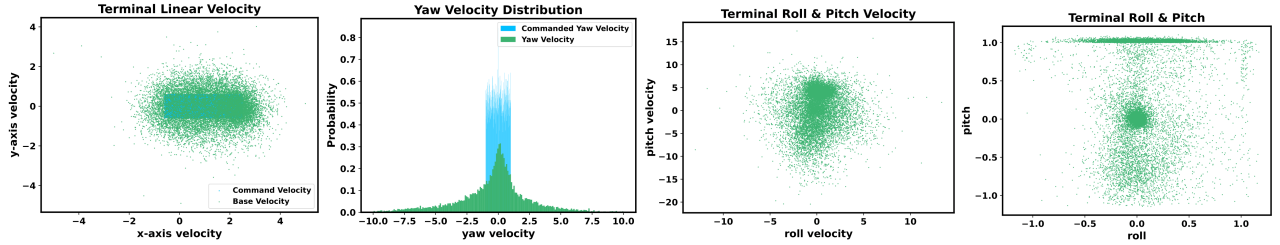


Figure 6. Extreme State: Policy’s state distribution in the extreme cases

A.5. PPO Algorithm

In order to enhance the understanding of historical observation information, we have made some improvements to the Actor-network. We first process this information using an encoder network to preliminarily extract the features of the observation values at each time step, and then use a merger network to integrate the observation values at different time steps. Finally, we obtain fixed-dimensional feature information, which is then input into the Actor backbone network together with other information.

Table 10. PPO hyperparameters

Hyperparameter	Value
Actor Layer	[512, 256, 128]
Critic Layer =	[512, 256, 128]
Discount Factor	0.99
GAE Parameter	0.95
Epochs per Rollout	5
Minibatch	4
Entropy Coefficient	0.005
Value Loss Coefficient (α_1)	1.0
Clip Range	0.2
Learning Rate	$2.e-4$
Environment Steps per Rollout	24

A.6. Discriminator

The input to the discriminator s^d is defined as $[q, v, w, r, p, k]$, where k represents the local positions of key points. Specifically, we define 12 key points, including the hips, shoulders, hands, ankles, knees, and elbows. For the Unitree H1, the total input dimension is 63, while for the Unitree G1, it is 67.

The discriminator’s hyperparameters are shown in Table. 11.

Table 11. Discriminator hyperparameters

Hyperparameter	Value
Discriminator Hidden Layer Dim	[1024,512]
Replay Buffer Size	500000
Expert Buffer Size	200000
Expert Fetch Size	512
Learning Batch Size	4096
Learning Rate	2e-5
Gradient Penalty Coefficient	1.0
lamda	1.0

A.7. Deployment Details

We utilize the Unitree H1 humanoid robot as our deployment platform. This full-sized humanoid robot weighs 47 kg, stands approximately 1.8 meters tall, and features 19 degrees of freedom. The control frequency is set to 100 Hz for both simulation and real-world deployment. The PD gains, characterized by stiffness and damping values, used in the real-world deployment are detailed in Table 12.

Table 12. Stiffness, Damping and Torque Limit

Joint Names	Stiffness [N*m/rad]	Damping [N*m*s/rad]	Torque Limit (Nm)
hip yaw	200	5	170
hip roll	200	5	170
hip pitch	200	5	170
knee	300	6	255
ankle	40	2	34
torso	200	5	170
shoulder	30	1	34
elbow	30	1	18

B. Experiment

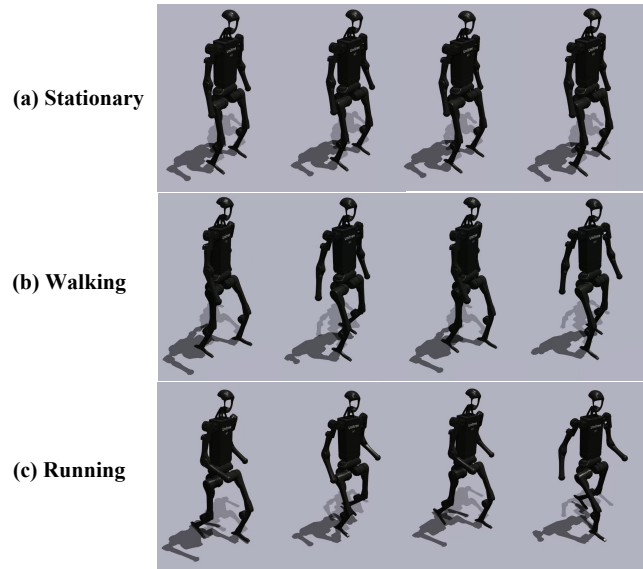


Figure 7. Human-like Behavior

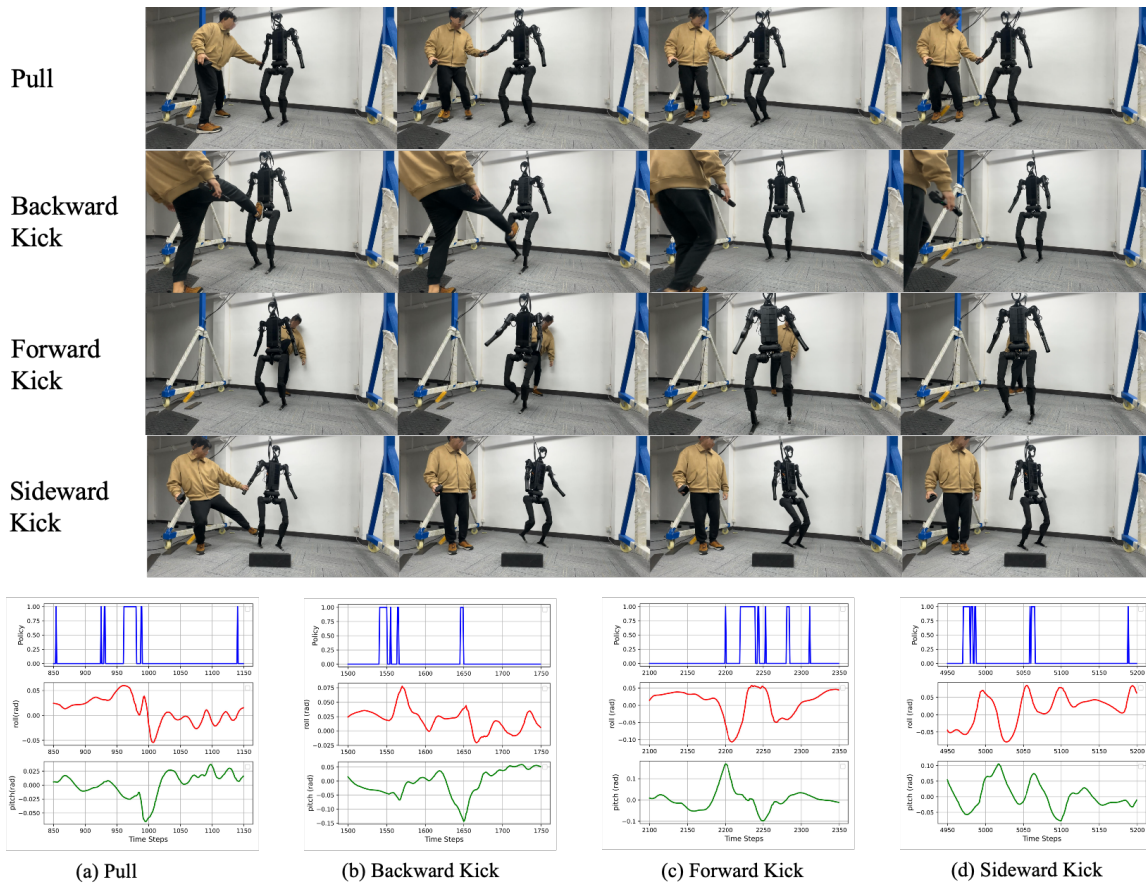


Figure 8. Disturbance: We apply various disturbances to Unitree H1 lasting for one minute. Four representative disturbance segments were selected for analysis. In these segments, a Policy Switching value of 0 corresponds to the goal-tracking policy, while a value of 1 denotes the safety recovery policy. The time is measured in control cycles, with each cycle lasting 0.01 seconds.

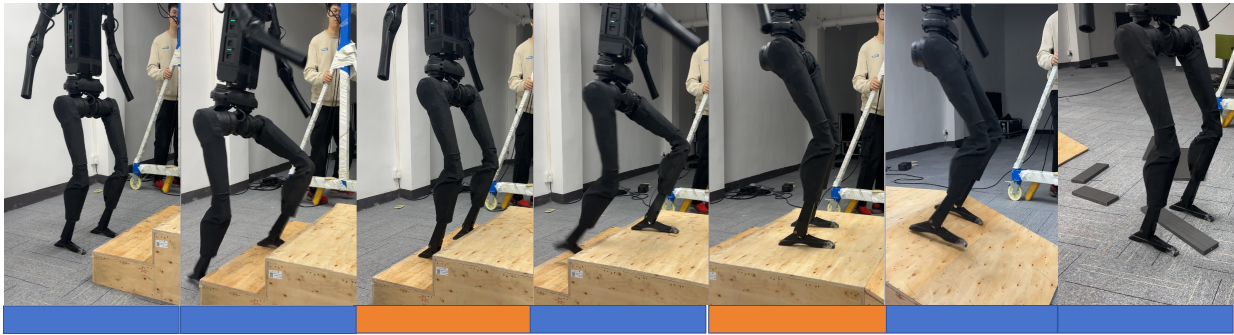


Figure 9. Parkour Test: The blue segment represents the goal-tracking policy, while the orange segment signifies the safety recovery policy.